metals

MDPI

Article

High-Resolution Characterization of Deformation Induced Martensite in Large Areas of Fatigued Austenitic Stainless Steel Using Deep Learning

Šárka Mikmeková [1,*], Jiří Man [2], Ondřej Ambrož [1], Patrik Jozefovič [1], Jan Čermák [1], Antti Järvenpää [3], Matias Jaskari [3], Jiří Materna [4] and Tomáš Kruml [2]

1 Institute of Scientific Instruments, Czech Academy of Sciences, Královopolská 147, 612 00 Brno, Czech Republic; ondrej@isibrno.cz (O.A.); patjoz@isibrno.cz (P.J.); cermak@isibrno.cz (J.Č.)
2 Institute of Physics of Materials, Czech Academy of Sciences, Žižkova 22, 616 62 Brno, Czech Republic; man@ipm.cz (J.M.); kruml@ipm.cz (T.K.)
3 Kerttu Saalasti Institute, University of Oulu, 85500 Nivala, Finland; antti.jarvenpaa@oulu.fi (A.J.); matias.jaskari@oulu.fi (M.J.)
4 Machine Learning College, Chrlická 787/56, 620 00 Brno, Czech Republic; jiri@mlcollege.com
* Correspondence: sarka@isibrno.cz

Abstract: This paper aims to demonstrate a novel technique enabling the accurate visualization and fast mapping of deformation-induced α'-martensite produced during cyclic straining of a metastable austenitic stainless steel, refined by reversion annealing to different grain sizes. The technique is based on energy and angular separation of the signal electrons in a scanning electron microscope (SEM). Collection of the inelastic backscattered electrons emitted under high take-off angles from a sample surface results in the acquisition of micrographs with high sensitivity to structural defects, such as dislocations, grain boundaries, and other imperfections. The areas with a high density of lattice imperfections reduce the penetration depth of the primary electrons, and simultaneously affect the signal electrons leaving the specimen. This results in an increase in the inelastic backscattered electrons yielded from the vicinity of α'-martensite, and a bright halo surrounds this phase. The α'-martensite phase can thus be separated from the austenitic matrix in SEM micrographs. In this work, we propose a deep learning method for a precise α'-martensite mapping within a large area. Various deep learning-based methods have been tested, and the best result measured by both Dice loss and IoU scores has been achieved using the U-Net architecture extended by the ResNet encoder.

Keywords: scanning electron microscopy (SEM); austenitic stainless steel; low cycle fatigue; deformation induced martensite; deep learning

check for updates

Citation: Mikmeková, Š.; Man, J.; Ambrož, O.; Jozefovič, P.; Čermák, J.; Järvenpää, A.; Jaskari, M.; Materna, J.; Kruml, T. High-Resolution Characterization of Deformation Induced Martensite in Large Areas of Fatigued Austenitic Stainless Steel Using Deep Learning. *Metals* **2023**, *13*, 1039. https://doi.org/10.3390/met13061039

Academic Editor: Alain Pasturel

Received: 12 April 2023
Revised: 18 May 2023
Accepted: 23 May 2023
Published: 29 May 2023

Copyright: © 2023 by the authors. Licensee MDPI, Basel, Switzerland. This article is an open access article distributed under the terms and conditions of the Creative Commons Attribution (CC BY) license (https://creativecommons.org/licenses/by/4.0/).

1. Introduction

Austenitic stainless steels (ASSs) are characterized by excellent formability, work hardening and weldability, and good corrosion resistance, and thus within the stainless steel family still occupy a privileged position [1]. Due to their combination of prominent mechanical and technological properties, they have found uses in diverse industrial, domestic, architectonic and biological applications [2–4]. In addition to the classical well-known Cr–Ni AISI 300 ASS grades, great attention has recently also been paid to their leaner alloyed equivalent, so-called TRIP/TWIP (transformation-induced plasticity/twin induced plasticity) Cr–Mn–Ni steels [5].

In the annealed state, these steels have a fully austenitic microstructure, which is responsible for their excellent ductility but limited yield strength. The parent fcc (face centered cubic) paramagnetic austenitic γ structure of most of these steels is known to be, however, metastable. Thus, depending on the ASS stability, it can partially transform to ferromagnetic bcc (body centered cubic) α'-martensite spontaneously during cooling, and/or

athermally by mechanical straining; for a recent review, see [6–8]. Generally, the stability of ASSs and their susceptibility to deformation-induced martensite (DIM) formation depends primarily on the chemical composition and temperature—see the two well-known characteristic threshold temperatures designated as M_s and M_{d30}, which can be calculated using empirically derived equations from the chemical composition (see e.g., [4,9]). An important factor that has a crucial effect on the nucleation mechanisms, morphology and kinetics of DIM formation is the stacking fault energy (SFE) [10–12]. Since SFE alone depends on the chemical composition and temperature [6,7,12–14], the deformation/hardening behavior of metastable ASSs is also strongly temperature-dependent, and is dictated by the dominant deformation mechanisms for a given temperature [7,8,11].

Deformation-induced martensitic transformation and its impact on the deformation behavior of ASSs during monotonic or cyclic loading via the TRIP or TRIP/TWIP effect has been the subject of numberless studies; for a recent review, see [6,8,11,12,15,16]. Among other areas in which the role of DIM is of outstanding importance, we may include (i) grain refinement via reversion annealing after prior cold working [8,17,18], (ii) magnetic stability at cryogenic temperatures (superconducting magnets) [19,20], (iii) non-destructive monitoring of fatigue damage and assessment of residual fatigue life [21–25], (iv) delayed cracking after deep drawing of lean-nickel alloyed ASSs [26,27], (v) the role of DIM in hydrogen environment embrittlement [28–32], and (vi) pitting corrosion and stress corrosion behavior [33–36].

Numerous characterization techniques can be utilized for the characterization and quantitative assessment of deformation-induced ε- and α′-martensite phases in austenitic steels; for comprehensive reviews see [6,8,11,37–39]. X-ray diffraction (XRD), ferritescope, optical microscopy (OM) and electron back-scattered diffraction (EBSD) are the most common techniques used to detect and quantify the martensite phase induced by static or cyclic deformation. XRD measurement offers information about the martensite phase content, but not about its size and distribution within a matrix. The same is true also for a more local ferritescope, which, in principle, can detect only a ferromagnetic phase, i.e., α′-martensite and/or possible δ-ferrite. The OM technique enables one to visualize the martensite phase. The specimens used for OM analysis have to be specially etched to reveal martensite, which is tricky, especially in the case of large areas. Moreover, the spatial resolution of the OM is limited and insufficient for the visualization of fine martensite phases. The EBSD technique enables the visualization and separation of all phases in steel with relatively high spatial resolution [40]. On the other hand, this technique requires a high-quality metallographic specimen. Furthermore, EBSD analysis with a suitable resolution is time-consuming, and is absolutely impracticable in the characterization of spacious areas on the specimen's surface. A scanning electron microscope (SEM) enables high spatial resolution together with fast data acquisition. Unfortunately, the phases in multiphase steels are not distinguishable in conventional SEM micrographs without any special etching of the specimen surface. Even after selective etching, some fine phases are hard to identify. Transmission electron microscopy (TEM) provides sub-nanometer spatial resolution and precise phase identification by means of electron diffraction. On the other hand, TEM requires special specimens in the form of very thin foils. Preparation of the TEM specimens is extremely cost- and time-consuming, and only local information about the material can be obtained. In fact, there is no method for the precise high-resolution mapping of deformation-induced martensite over large areas.

In this work, we propose a novel technique with high spatial resolution intended for large-area mapping of α′-martensite phase generated in cyclically strained fine-grained metastable 301LN austenitic stainless steel. Experimental data obtained in the bulk of fatigued 301LN steel are compared with our recent results of surface observations using different microscopic techniques applied to the identical material cyclically strained to the early stages of fatigue life [41].

2. Materials and Methods

A commercial metastable 301LN austenitic stainless steel sheet with the chemical composition (in wt.%) 0.025 C, 0.53 Si, 1.25 Mn, 0.024 P, 0.001 S, 17.5 Cr, 6.5 Ni, 0.2 Cu, 0.09 Mo, and 0.15 N, with the rest being Fe, was submitted to so-called fast reversion annealing after prior cold deformation at the University of Oulu. This specific thermomechanical treatment is recognized as an effective tool for grain refinement and the considerable improvement of tensile properties (for the most recent comprehensive review on this topic see [18]). Annealing at 1050 °C/200 s and 900 °C/1 s resulted in a coarse-grained (CGA1) and fine-grained (FGA) fully austenitic microstructure with average grain sizes of 13 µm and 1.4 µm, respectively. The flat dog-bone 3 mm thick specimens with a gauge width and length of 4 mm and 6 mm, respectively (see Figure 1), were cyclically strained in a symmetrical push–pull cycle at room temperature, with a constant total strain amplitude of 0.5%, to a very early stage of fatigue life. After completion of the fatigue tests the gauge part of the specimens was sectioned by spark-erosion both longitudinally and transversally (see Figure 1). For microstructure investigations, the sections were carefully polished mechanically and electrolytically using solution A2 (Struers GmbH, Roztoky u Prahy, Czech Republic) consisting of 78 mL perchloric acid, 120 mL distilled water, 700 mL ethanol and 100 mL butyl cellosolve (butyl glycol) at ambient temperature and at a current of less than 5 A for 1 min. Other details on the material and its thermomechanical treatment as well as low-cycle fatigue tests can be found elsewhere [41–43].

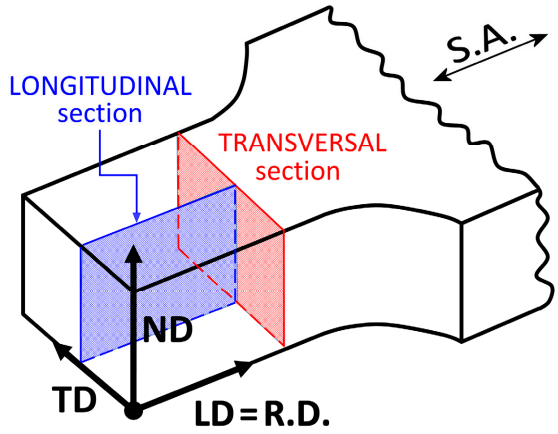


Figure 1. Schema of fatigue specimen geometry with indicated longitudinal and transversal sections used for the large-area microstructure mapping (S.A. = stress axis, R.D. = rolling direction, LD = longitudinal direction, TD = transversal direction, ND = normal direction).

The specimens were investigated using an extreme high-resolution scanning electron microscope (SEM) MagellanTM 400 L (Thermofisher Scientifics, Waltham, MA, USA) enabling sub-nanometer spatial resolution. The instrument is equipped with a multiple detection system. The signal electrons can be collected by a through-the-lens (TLD) detector, a conventional Everhart–Thornley detector (ETD), and a multi-segment solid state high-efficiency back-scattered electron (CBS) detector. The TLD and the ETD detectors are designated for detection of the secondary electrons (SEs) and the CBS detector collects the back-scattered electrons (BSEs). The instrument is described in detail elsewhere [44]. In this study, the CBS detector [45] was utilized for inelastic BSEs signal collection. The microscope is equipped with an electron back-scattered diffraction (EBSD) detector Hikari (EDAX, Pleasanton, CA, USA) paired with EDAX's TEAM^{TM} EBSD analysis system software (Version 4.0). The EBSD maps were analyzed with the OIM 7 software. MAPS software version 2.0 (Thermofisher Scientific, Waltham, MA, USA) was used for the automated acquisition of high-resolution images from a large area [46]. The arrangement of detectors with respect to specimen position inside the microscope chamber is shown in Figure 2.

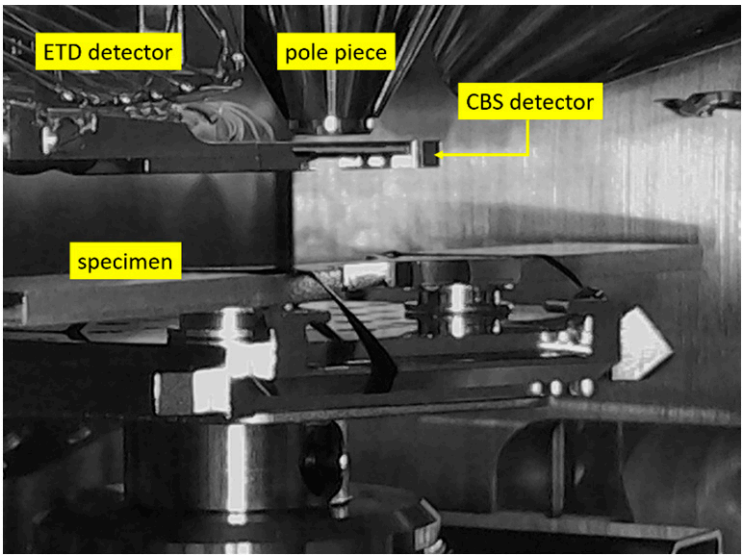


Figure 2. A view inside the chamber of high-resolution SEM Magellan 400 L.

3. Results and Discussion

3.1. Visualization of Martensite Phase in SEM Micrographs

Figure 3 shows SEM micrographs taken within the area located in the middle of the transversal section of the coarse-grained 301LN steel specimen (see Figure 1) cyclically strained to the very early stage of fatigue life and corresponding phase EBSD map. The SEM micrographs were obtained under various imaging conditions and detection geometries. Figure 3a shows the SEM micrograph captured by the TLD detector. This image as created mainly from the true SEs and is surface-sensitive. One can observe surface imperfections, contamination, and a weak crystallographic contrast; however, without any detectable contrast discriminating the microstructural phases. Figure 3b represents a BSE micrograph collected by the CBS detector. The micrograph is created mainly by the elastic low take-off angle BSEs, which was secured using a very short work distance and low impact energy of the primary beam. The image primarily exhibits the channeling contrast. Clear distinctions between the martensite phase and the austenitic matrix are impossible. Figure 3c also represents a BSE image similar to that in Figure 3b, but in this case it is created by the inelastic high take-off angle BSEs. As is apparent from this figure, the martensite phase imaged under this condition exhibits a bright contrast caused by an intensive reflection of signal electrons. The bright areas correspond to α'-martensite phase particles, as verified by the EBSB mapping of the corresponding area shown in Figure 3d. This phenomenon has been already observed in complex steels, as reported elsewhere [47,48], where optimal SEM conditions securing the clear contrast between the martensite and other phases were provided. The inelastic high take-off angle BSEs were assigned as a source of the contrast. The origin of the contrast is attributed to the sensitivity of the high-loss BSEs on structural imperfections, namely on dislocations inside the martensite phase. The discontinuity of crystal potential in the vicinity of dislocations results in a dramatic increase in the rate of electrons scattered by phonons. The electron–photon interaction has a quasi-elastic character, and the momentum transfer is large. It results in a reduction in the coherence of the primary electron wave and suppresses the transmission of the primary electron beam. These factors, i.e., the enhanced electron scattering from dislocation-rich areas and the suppressed penetration depth of the primary beam, result in a high yield of backscattered electrons from α'-martensite.

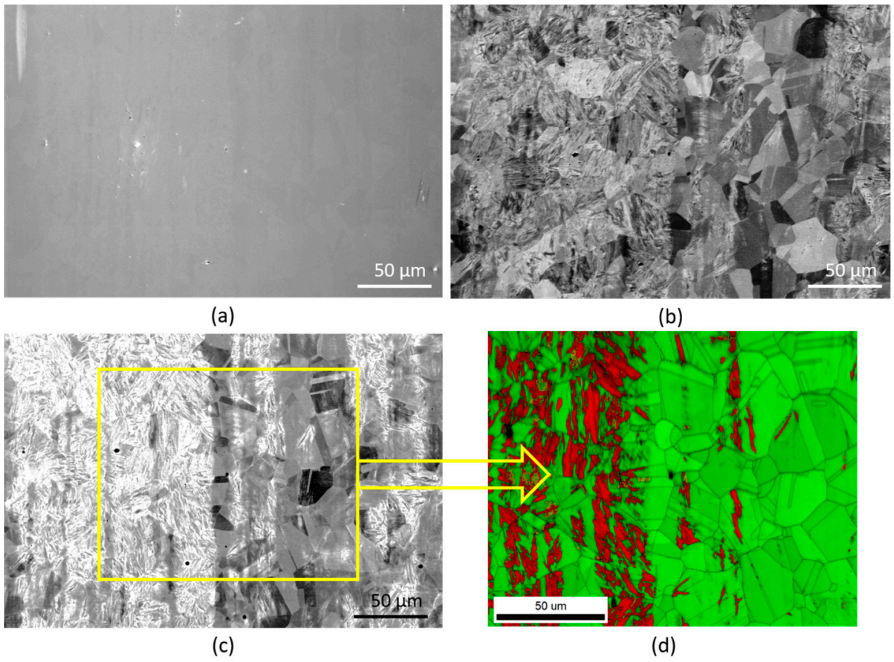


Figure 3. Area within central part of transversal section of fatigued coarse-grained 301LN steel (cf. Figure 1) imaged under various imaging conditions in SEM: (**a**) the SE micrograph captured at 5 keV primary beam energy by the TLD detector, (**b**) the elastic BSE micrograph obtained at 5 keV primary beam energy by the CBS detector using short working distance, (**c**) the inelastic BSE micrograph acquired at 30 keV primary beam energy using the CBS detector and long working distance securing collection of the high take-off angle signal electrons, (**d**) EBSD phase + image quality map (green color = austenite, red color = α'-martensite, and yellow color = ε-martensite).

Figure 4a shows an SEM micrograph obtained under conditions securing the collection of the high-loss, high-take-off angle BSE signal. As is visible, the source of the extremely strong signal illuminates not only α'-martensite itself but also its vicinity. As reported earlier [49], the martensite phase induces volume changes compared to the parent austenite, and α'-martensite generates a volume expansion of 2.57%, which is inseparably connected with the presence of structural defects. Moreover, favorable nucleation sites of α'-martensite are dislocation pile-ups. The presence of structural defects in the vicinity of the α'-martensite phase is a source of a bright halo around this phase. Thus, due to this effect, the α'-martensite can be easily identified in the SEM micrographs created by the inelastic BSEs.

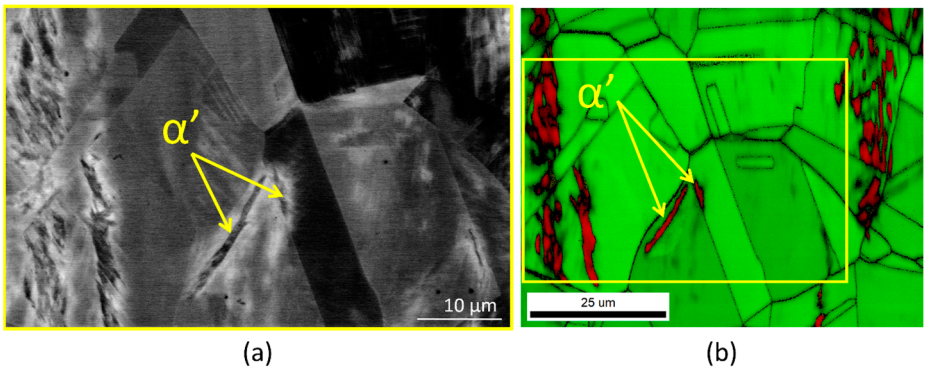


Figure 4. (**a**) High-loss BSE SEM micrograph of fatigued coarse-grained 301LN steel obtained at 30 keV primary beam energy by the CBS detector together with (**b**) corresponding EBSD phase + image quality map (green color = austenite, red color = α'-martensite).

3.2. Large-Area Mapping: Automated Image Acquisition in the SEM

As mentioned above, the SEM micrographs obtained under the conditions securing the collection of high-take-off angle, high-loss BSEs enable the separation of the α'-martensite phase from the austenitic matrix. This was utilized for large-area mapping in the SEM. The image acquisition process was automated using the software MAPS 2 (Thermofisher Scientific, Waltham, MA, USA). Figure 5 shows an example of MAPS data collected from the specimen. The high-resolution SEM micrographs of 1024 × 884 pixels size were collected automatically over the entire surface of the specimen section, with a 10% overlap. The SEM images were acquired at 30 keV primary beam energy by the CBS detector, which enables the collection of inelastic BSEs. In order to improve the contrast between α'-martensite and the matrix, the detection of the high-take-off angle BSEs was reached by utilizing a large working distance. The distance between the specimen's surface and the detector was over 12 mm. The long working distance reduced the detection efficiency of the CBS detector, and a very high probe current was used to improve signal/noise ratio. The probe current was set to 26 nA.

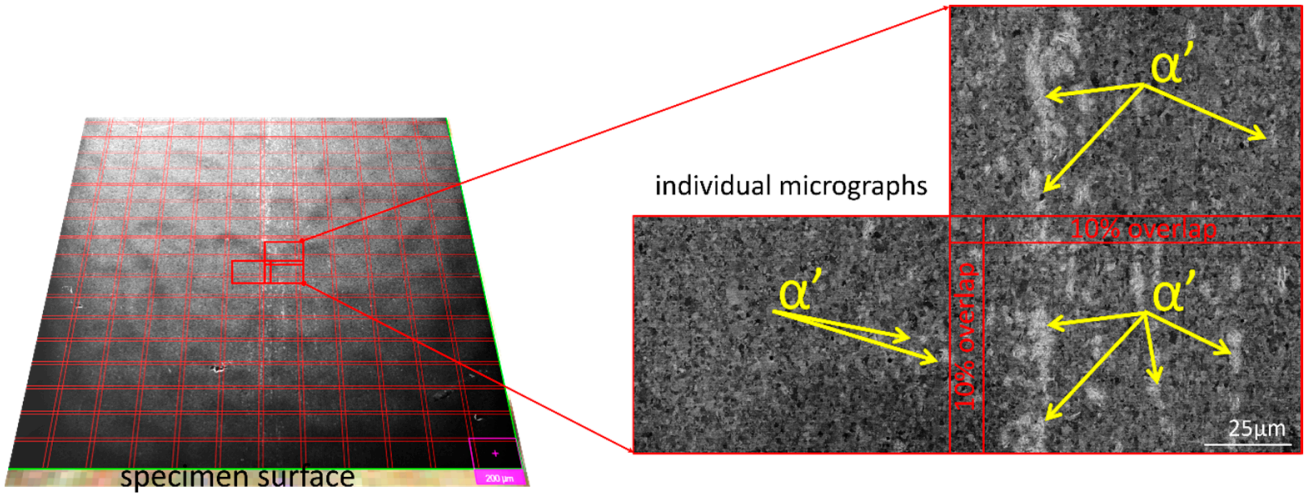


Figure 5. Automated data acquisition by means of the MAPS software applied to the specimen section of fatigued fine-grained 301LN steel.

Figure 6 shows montaged high-resolution SEM micrographs of the longitudinal and transversal specimen sections (cf. Figure 1). The SEM micrographs were obtained under the conditions described above, i.e., 30 keV landing energy of the primary electrons, working distance of 12 mm, and the probe current of 26 nA. After stitching, the longitudinal section map represents an image of 19,754 × 29,280 pixels and 16,850 × 26,331 pixels in the case of the transversal specimen section. The bright contrast represents the areas containing the α'-martensite. Unfortunately, the α'-martensite is not the only source of the extraordinarily bright contrast in the SEM micrograph, but dirt, dust and sample preparation artifacts are also connected with this type of contrast. This highlights the necessity of taking the utmost care during surface preparation.

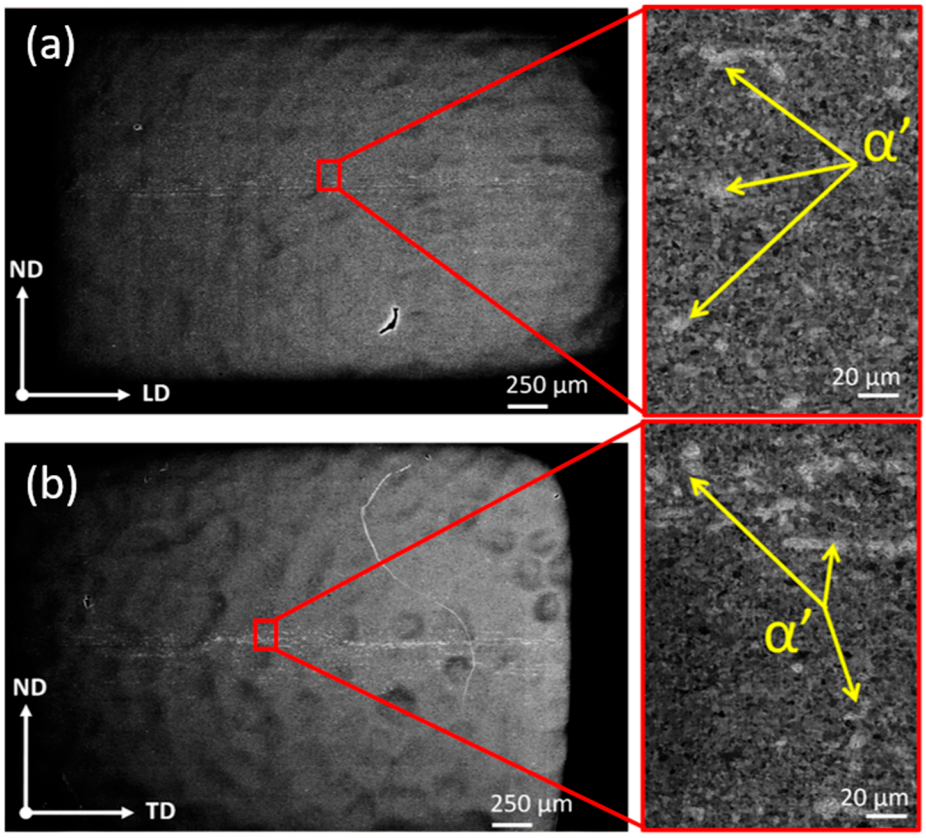


Figure 6. The microstructure of fine-grained 301LN steel cyclically strained to the very early stage of fatigue life within (**a**) longitudinal and (**b**) transversal specimen section as obtained by SEM-automated data acquisition. The stitched image of the longitudinal section comprises 32 × 14 SEM micrographs and the transversal section 29 × 12 SEM micrographs. The size of each SEM micrograph is 1024 × 884 pixels. Details indicated by red rectangles in both specimen sections correspond to an individual SEM micrograph, i.e., a tile from which the large SEM images of specimen sections were composed.

3.3. Deep Learning

Identification of the α'-martensite in the SEM micrographs in the section maps shown in Figure 5 by a simple thresholding is not possible due to the inhomogeneous illumination and the presence of impurities on the surface. Therefore, we propose to use an extension of the U-Net architecture [50] for the segmentation of α'-martensite in SEM micrographs obtained automatically in the software MAPS (Figure 5). Convolutional neural networks (CNN) have been broadly used for the image classification task, where the input dimension reflects the shape of images and the number of outputs corresponds to the number of predicted classes [51,52]. Long et al. [53] proposed a fully convolutional neural network that takes an input of arbitrary size and produces a correspondingly sized output with efficient inference and learning. This architecture can be used for image-to-image translation, where the input is a microscopy image and the output is a mask of the same size. Each pixel of this mask represents the occurrence probability of α'-martensite on the same position in the input. The main idea in fully convolutional networks is to supplement a typical contracting network by successive layers, where the pooling operators are replaced by up-sampling operators. In the U-Net architecture, which stems from fully convolutional networks, the up-sampling parts additionally have a large number of feature channels, which allow the network to propagate contextual information to higher-resolution layers. As a consequence, the expansive path is more or less symmetrical to the contracting path, and yields a U-shaped architecture. The network does not have any fully connected layers and only uses the valid part of each convolution, i.e., the segmentation mask only contains

the pixels for which the full context is available in the input image. In the present work, the original U-net architecture has been extended via a pre-trained image encoder based on the ResNet model [54], which allows the network to better interpret the structures hidden in the input images. We have also experimented with other architectures, such as feature pyramid network (FPN) [55], LinkNet [56] and pyramid scene parsing (PSP)Net [57], and made a brief comparison. The whole data set of the individual SEM micrographs consisted of 796 tiles. From this data set, we have randomly picked 260 micrographs for which the segmentation masks have been created manually. An example of the manual segmentation of α'-martensite is shown in Figure 7. These 260 images have been randomly split to train (230 images) and validate (30 images) the data sets. All encoders of the models used for the experiments have been initialized with weights trained on the ImageNet data set [58] and then fine-tuned for our train data set. We have implemented all experiments in PyTorch [59] and optimized the models in 150 epochs against the Dice loss [60]. All results have been compared in terms of IoU score [61]—see Table 1. IoU score, which stands for "Intersection Over Union", is a standard evaluation metric used for segmentation evaluation. It measures the overlap of the predicted regions with the ground true regions as the proportion of their intersection and union. The results for both specimen sections are shown in Figure 8.

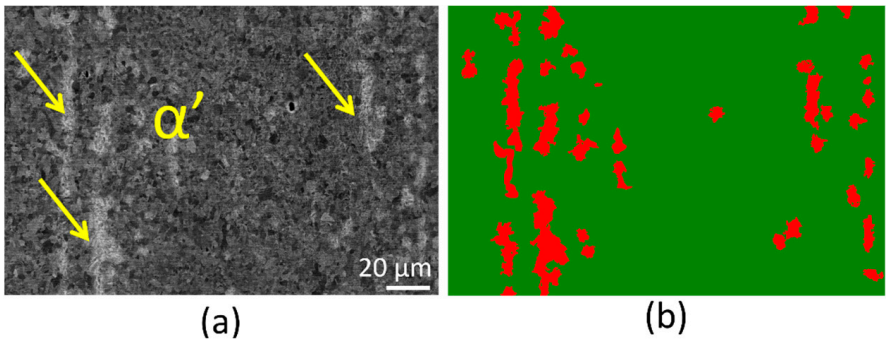


Figure 7. An example of manual α'-martensite segmentation: (**a**) an inelastic high-take-off angle BSE SEM micrograph and (**b**) a mask (green = austenite, red = martensite phase).

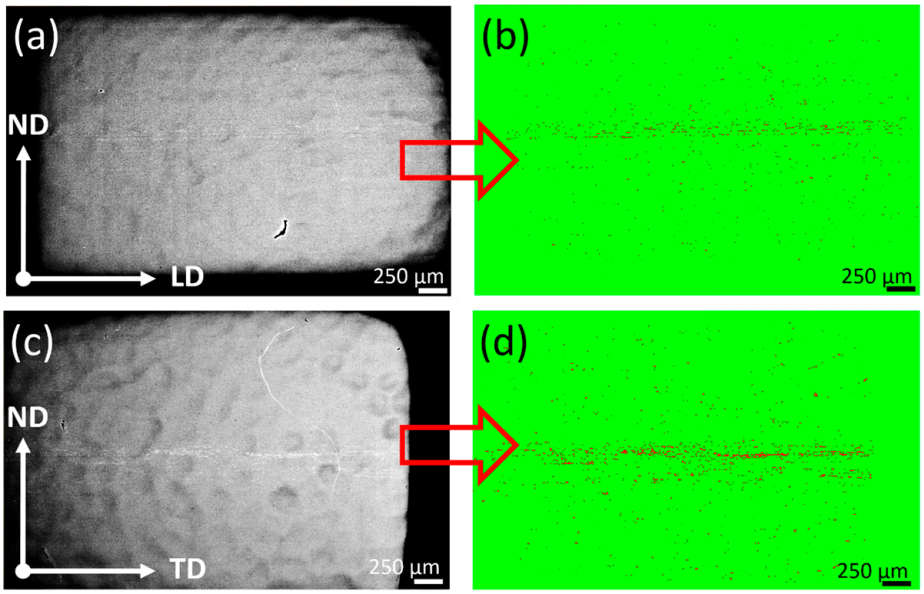


Figure 8. Montaged original SEM micrographs of the longitudinal (**a**) and transversal (**c**) specimen section together with the corresponding montaged images of the result of the α'-martensite segmentation (**b**,**d**), obtained using the deep learning method (green = austenite, red = α'-martensite phase).

Table 1. Evaluation of various neural network architectures in terms of Dice loss and IoU score.

Model	Best Validation Dice Loss	Best Validation IoU Score
U-net with ResNet encoder	0.3639	0.5436
FPN	0.8619	0.1379
Link Net	0.3958	0.5258
PSP Net	0.5853	0.3471

The results of the α′-martensite segmentation using the deep learning method described above are shown in Figure 9. The total analyzed area was about 8 mm^2 in both longitudinal and transversal specimen sections. The montaged images show extremely precise maps of the α′-martensite distribution within the austenite matrix. The black color represents the α′-martensite phase and the matrix forms a white background. It is clear from both specimen sections that the α′-martensite is not distributed uniformly across the specimen thickness. In agreement with our previous observations on the free surfaces of fatigued specimens [41], the considerably higher content of α′-martensite in the bulk of fatigued fine-grained 301LN steel during the early stage of cyclic straining is concentrated in the middle of the sheet's thickness. While α′-martensite particles outside the central part of the specimen's thickness are distributed more or less uniformly, a clear tendency towards forming α′-martensite islands in the form of thin bands is apparent in the middle of the specimen thickness. Quantitative analysis over the whole area of the specimens' sections (see Table 2) shows a slightly higher amount of the α′-martensite phase in the transversal section.

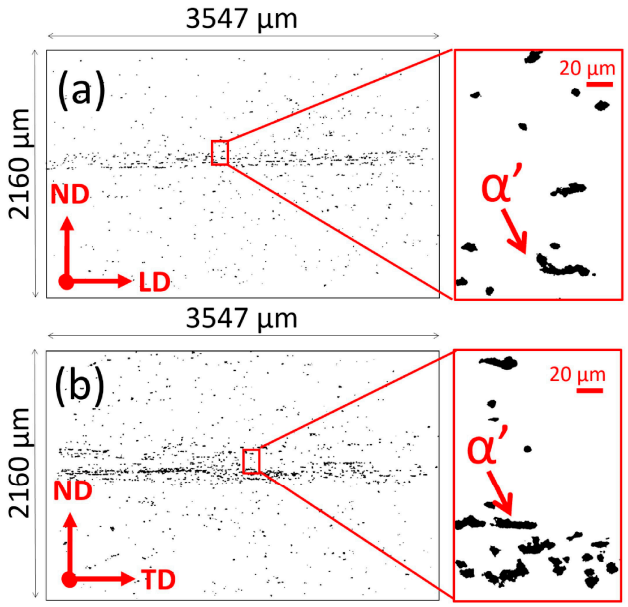


Figure 9. Distribution of α′-martensite within the austenite matrix in (**a**) longitudinal and (**b**) transversal sections of the gauge part of the flat specimen of the 301LN steel cyclically strained to the early stage of fatigue life.

Table 2. Fraction of α′-martensite within the whole area of two sections across the gauge part of the specimen of 301LN steel fatigued to the very early stage of fatigue life.

Section	Analyzed Area (mm^2)	α′-Martensite Fraction
Longitudinal	7.97	0.931%
Transversal	7.97	1.298%

In order to quantitatively assess the variations in α′-martensite content across the sheet thickness, another methodology was applied to both specimen sections. As apparent from Figure 10a,b the α′-martensite fraction was evaluated within a 500 µm-wide stripe running through the specimen's thickness (i.e., parallel to ND), which was furthermore subdivided into 50 µm-thick slices. The results of the quantitative analysis of specimen cross-sections presented in Figure 10c are consistent with our recent examinations using optical microscopy (Nomarski contrast) and EBSD on free surfaces within the gauge part of fatigued flat 301LN steel specimens, and they further support the suggested hypothesis on the origin of the characteristic changes in the hysteresis loop shape during the early stage of the cyclic straining of fine-grained 301LN steel [41].

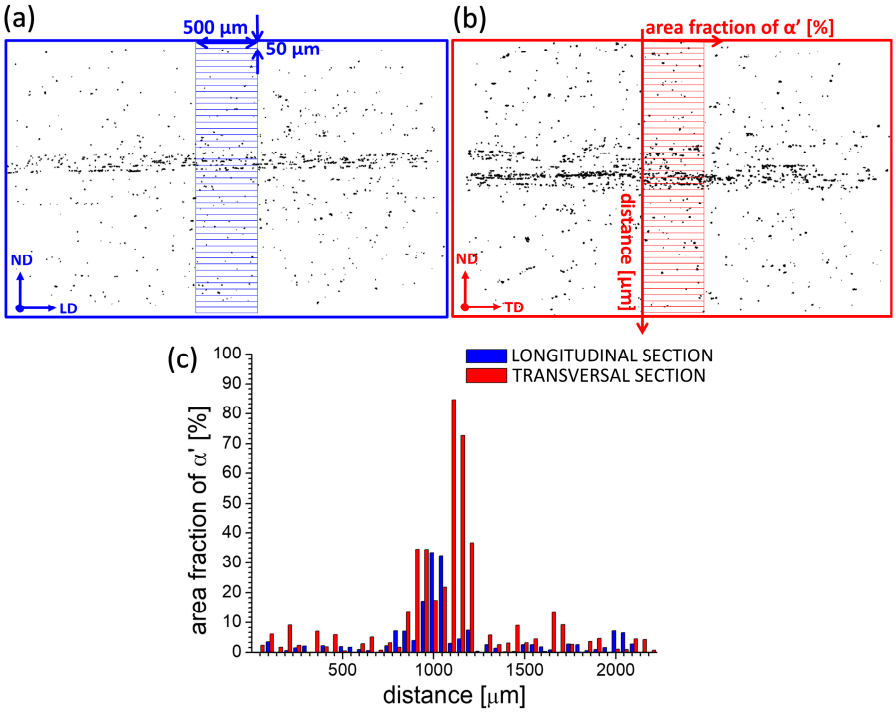


Figure 10. Methodology of quantitative evaluation of α′-martensite (black area) content across the thickness of fatigued flat 301LN steel specimen. The fraction of α′-martensite was assessed within rectangular areas 50 × 500 µm as indicated for (**a**) longitudinal and (**b**) transversal sections, and plotted for both sections as a function of distance from the specimen surface (**c**).

4. Summary and Conclusions

A novel technique enabling fast mapping of the α′-martensite distribution with a high spatial resolution and sensitivity within a large area of specimen sections has been proposed. The technique is based on the acquisition of SEM micrographs obtained under special conditions, where only the inelastic high-take-off angle BSEs are collected. These micrographs are sensitive to the presence of structural defects, such as dislocations and lattice distortion. The presence of α′-martensite particles in the austenite matrix is connected with a volume expansion, which results in a discontinuity of crystal potential. The discontinuity of crystal potential drastically increases the rate of electrons scattered by phonons. This electron–phonon interaction leads to a large momentum transfer and the coherence of the primary electron wave is reduced. It suppresses the transmission of the primary electrons and increases their back-scattering coefficient. This phenomenon causes the presence of a bright contrast around the α′-martensite phase, which allows the separation of this phase from the austenite matrix in SEM micrographs created by the high-loss BSEs. The SEM technique is suitable for large-area mapping due to its fast data acquisition. The collection of high-quality SEM micrographs takes only a few seconds. Moreover, the image acquisition process can be automated by means of special software, such as MAPS in our case.

In this work, the microstructure of fine-grained 301LN stainless steel cyclically strained to the early stage of fatigue life was characterized in order to obtain precise data on the destabilization of an originally fully austenitic structure and the distribution of α'-martensite within the austenitic matrix. The microstructure measurements were performed on two different sections within the gauge part of the flat dog-bone-shaped fatigued specimens, namely, on a longitudinal section and a transverse section. The high-loss BSEs micrographs were automatically collected from the whole specimen sections, and these micrographs containing bright contrast around the α'-martensite phase were utilized as a source for subsequent image processing using a deep learning method.

Various deep learning-based models were tested for image segmentation with respect to the identification of α'-martensite particles in the SEM images of 301LN steel. The best results measured by both Dice loss and IoU score were achieved by the U-Net architecture, extended by the ResNet encoder. This method enabled the precise mapping of the α'-martensite particles generated during cyclic straining over a large area with a high-spatial resolution.

Author Contributions: Conceptualization, Š.M. and J.M. (Jiří Man); methodology, J.M. (Jiří Man), Š.M., J.M. (Jiří Materna), T.K., A.J., and M.J.; validation, Š.M., O.A., P.J., J.Č., A.J. and M.J.; data cu-ration, O.A., J.Č., J.M. (Jiří Materna), and P.J.; writing—original draft preparation, Š.M.; writing—review and editing, J.M. (Jiří Man); supervision, T.K.; funding acquisition, Š.M. All authors have read and agreed to the published version of the manuscript.

Funding: This research was funded by the Czech Academy of Sciences, Strategy AV21: research program "New Materials Based on Metals, Ceramics and Composites".

Data Availability Statement: Not applicable.

Acknowledgments: The authors would like to thank Patrik Jozefovič for his help with data processing.

Conflicts of Interest: The authors declare no conflict of interest.

References

1. Boniardi, M.; Casaroli, A. *Stainless Steels*; Lucefin S.p.A.: Esine, Italy, 2014.
2. Lacombe, P.; Baroux, B.; Beranger, G. (Eds.) *Stainless Steels*; Les Editions de Physique: Les Ulis, France, 1993.
3. McGuire, M.F. *Stainless Steels for Design Engineers*; ASM International: Materials Park, OH, USA, 2008.
4. Lo, K.H.; Shek, C.H.; Lai, J.K.L. Recent developments in stainless steels. *Mater. Sci. Eng. R Rep.* **2009**, *65*, 39–104. [CrossRef]
5. Biermann, H.; Aneziris, C.G. (Eds.) *Austenitic TRIP/TWIP Steels and Steel-Zirconia Composites*; Springer Series in Materials Science 298; Springer Nature: Cham, Switzerland, 2020.
6. Hedström, P.; Odqvist, J. Deformation-induced martensitic transformation in metastable austenitic stainless steels–Introduction and current perspectives. In *Stainless Steel: Microstructure, Mechanical Properties and Methods of Application*; Pramanik, A., Basak, A.K., Eds.; Nova Science Publishers: New York, NY, USA, 2015; pp. 81–106.
7. de Bellefon, G.M.; Van Duysen, J.C. Tailoring plasticity of austenitic stainless steels for nuclear applications: Review of mechanisms controlling plasticity of austenitic steels below 400 °C. *J. Nucl. Mater.* **2016**, *475*, 168–191. [CrossRef]
8. Sohrabi, M.J.; Naghizadeh, M.; Mirzadeh, H. Deformation-induced martensite in austenitic stainless steels: A review. *Arch. Civ. Mech. Eng.* **2020**, *20*, 124. [CrossRef]
9. Hahnenberger, F.; Smaga, M.; Eifler, D. Microstructural investigation of the fatigue behavior and phase transformation in metastable austenitic steels at ambient and lower temperatures. *Int. J. Fatigue* **2014**, *69*, 36–48. [CrossRef]
10. Tian, Y.E.; Gorbatov, O.I.; Borgenstam, A.; Ruban, A.V.; Hedström, P. Deformation microstructure and deformation-induced martensite in austenitic Fe-Cr-Ni alloys depending on stacking fault energy. *Metall. Mater. Trans. A* **2017**, *48*, 1–7. [CrossRef]
11. Rafaja, D.; Ullrich, C.; Motylenko, M.; Martin, S. Microstructure aspects of the deformation mechanisms in metastable austenitic steels. In *Austenitic TRIP/TWIP Steels and Steel-Zirconia Composites: Design of Tough, Transformation-Strengthened Composites and Structures*; Chapter 11; Biermann, H., Aneziris, C.G., Eds.; Springer Series in Materials Science 298; Springer Nature: Cham, Switzerland, 2020; pp. 325–377.
12. Talonen, J.; Hänninen, H. Formation of shear bands and strain-induced martensite during plastic deformation of metastable austenitic stainless steels. *Acta Mater.* **2007**, *55*, 6108–6118. [CrossRef]
13. Martin, S.; Fabrichnaya, O.; Rafaja, D. Prediction of the local deformation mechanisms in metastable austenitic steels from the local concentration of the main alloying elements. *Mater. Lett.* **2015**, *159*, 484–488. [CrossRef]
14. Walter, M.; Mujica Roncery, L.; Weber, S.; Leich, L.; Theisen, W. XRD measurement of stacking fault energy of Cr–Ni austenitic steels: Influence of temperature and alloying elements. *J. Mater. Sci.* **2020**, *55*, 13424–13437. [CrossRef]

15. Man, J.; Smaga, M.; Kuběna, I.; Eifler, D.; Polák, J. Effect of metallurgical variables on the austenite stability in fatigued AISI 304 type steels. *Eng. Fract. Mech.* **2017**, *185*, 139–159. [CrossRef]
16. Weidner, A. *Deformation Processes in TRIP/TWIP Steels: In-Situ Characterization Techniques*; Springer Series in Materials Science 295; Springer Nature: Cham, Switzerland, 2020.
17. Somani, M.C.; Juntunen, P.; Karjalainen, L.P.; Misra, R.D.K.; Kyröläinen, A. Enhanced mechanical properties through reversion in metastable austenitic stainless steels. *Metall. Mater. Trans. A* **2009**, *40*, 729–744. [CrossRef]
18. Järvenpää, A.; Jaskari, M.; Kisko, A.; Karjalainen, P. Processing and properties of reversion-treated austenitic stainless steels. *Metals* **2020**, *10*, 281. [CrossRef]
19. Tobler, R.L.; Nishimura, A.; Yamamoto, J. Design-relevant mechanical properties of 316-type steels for superconducting magnets. *Cryogenics* **1997**, *37*, 533–550. [CrossRef]
20. Nishimura, A.; Ono, Y.; Umezawa, O.; Kumagai, S.; Kato, Y.; Kato, T.; Yuri, T.; Komatsu, M. Study on development policy for new cryogenic structural material for superconducting magnet of fusion reactor. *Nucl. Mater. Energy* **2022**, *30*, 101125. [CrossRef]
21. De Backer, F.; Schoss, V.; Maussner, G. Investigations on the evaluation of the residual fatigue life-time in austenitic stainless steels. *Nucl. Eng. Des.* **2001**, *206*, 201–219. [CrossRef]
22. Leber, H.J.; Niffenegger, M.; Tirbonod, B. Microstructural aspects of low cycle fatigued austenitic stainless tube and pipe steels. *Mater. Charact.* **2007**, *58*, 1006–1015. [CrossRef]
23. Smaga, M.; Walther, F.; Eifler, D. Deformation-induced martensitic transformation in metastable austenitic steels. *Mater. Sci. Eng. A* **2008**, *483–484*, 394–397. [CrossRef]
24. Mishakin, V.; Gonchar, A.; Kurashkin, K.; Kachanov, M. Prediction of fatigue life of metastable austenitic steel by a combination of acoustic and eddy current data. *Int. J. Fatigue* **2020**, *141*, 105846. [CrossRef]
25. Acosta, R.; Heckmann, K.; Sievers, J.; Schopf, T.; Bill, T.; Starke, P.; Donnerbauer, K.; Lücker, L.; Walther, F.; Boller, C. Microstructure-based lifetime assessment of austenitic steel AISI 347 in view of fatigue, environmental conditions and NDT. *Appl. Sci.* **2021**, *11*, 11214. [CrossRef]
26. Guo, X.; Post, J.; Groen, M.; Bleck, W. Stress oriented delayed cracking induced by dynamic martensitic transformation in meta-stable austenitic stainless steels. *Steel Res. Int.* **2011**, *82*, 6–13. [CrossRef]
27. Papula, S.; Talonen, J.; Hänninen, H. Effect of residual stress and strain-induced α'-martensite on delayed cracking of metastable austenitic stainless steels. *Metall. Mater. Trans. A* **2014**, *45*, 1238–1246. [CrossRef]
28. San Marchi, C.; Michler, T.; Nibur, K.A.; Somerday, B.P. On the physical differences between tensile testing of type 304 and 316 austenitic stainless steels with internal hydrogen and in external hydrogen. *Int. J. Hydrog. Energy* **2010**, *35*, 9736–9745. [CrossRef]
29. Egels, G.; Roncery, L.M.; Fussik, R.; Theisen, W.; Weber, S. Impact of chemical inhomogeneities on local material properties and hydrogen environment embrittlement in AISI 304L steels. *Int. J. Hydrog. Energy* **2018**, *43*, 5206–5216. [CrossRef]
30. Izawa, C.; Wagner, S.; Deutges, M.; Weber, S.; Pargeter, R.; Michler, T.; Uchida, H.H.; Gemma, R.; Pundt, A. Relationship between hydrogen embrittlement and M_{d30} temperature: Prediction of low-nickel austenitic stainless steel's resistance. *Int. J. Hydrog. Energy* **2019**, *44*, 25064–25075. [CrossRef]
31. Barrera, O.; Bombac, D.; Chen, Y.; Daff, T.D.; Galindo-Nava, E.; Gong, P.; Haley, D.; Horton, R.; Katzarov, I.; Kermode, J.R.; et al. Understanding and mitigating hydrogen embrittlement of steels: A review of experimental, modelling and design progress from atomistic to continuum. *J. Mater. Sci.* **2018**, *53*, 6251–6290. [CrossRef] [PubMed]
32. Qiu, Y.; Yang, H.; Tong, L.; Wang, L. Research progress of cryogenic materials for storage and transportation of liquid hydrogen. *Metals* **2021**, *11*, 1101. [CrossRef]
33. de Abreu, H.F.G.; de Carvalho, S.S.; de Lima Neto, P.; dos Santos, R.P.; Freire, V.N.; de Oliveira Silva, P.M.; Tavares, S.S.M. Deformation induced martensite in an AISI 301LN stainless steel: Characterization and influence on pitting corrosion resistance. *Mater. Res.* **2007**, *10*, 359–366. [CrossRef]
34. Lv, J.; Luo, H. Effects of strain and strain-induced α'-martensite on passive films in AISI 304 austenitic stainless steel. *Mater. Sci. Eng. C* **2014**, *34*, 484–490. [CrossRef]
35. Solomon, N.; Solomon, I. Effect of deformation-induced phase transformation on AISI 316 stainless steel corrosion resistance. *Eng. Fail. Anal.* **2017**, *79*, 865–875. [CrossRef]
36. Silva, P.M.; Filho, M.C.; Cruz, J.A.D.; Sales, A.J.; Sombra, A.S.; Tavares, J.M.R. Influence on pitting corrosion resistance of AISI 301LN and 316L stainless steels subjected to cold-induced deformation. *Metals* **2023**, *13*, 443. [CrossRef]
37. Talonen, J.; Aspegren, P.; Hänninen, H. Comparison of different methods for measuring strain induced α'-martensite content in austenitic steels. *Mater. Sci. Technol.* **2004**, *20*, 1506–1512. [CrossRef]
38. Haušild, P.; Davydov, V.; Drahokoupil, J.; Landa, M.; Pilvin, P. Characterization of strain-induced martensitic transformation in a metastable austenitic stainless steel. *Mater. Des.* **2010**, *31*, 1821–1827. [CrossRef]
39. Celada-Casero, C.; Kooiker, H.; Groen, M.; Post, J.; San-Martin, D. In-situ investigation of strain-induced martensitic transformation kinetics in an austenitic stainless steel by inductive measurements. *Metals* **2017**, *7*, 271. [CrossRef]
40. Carneiro, Í.; Simões, S. Recent advances in EBSD characterization of metals. *Metals* **2020**, *10*, 1097. [CrossRef]
41. Man, J.; Järvenpää, A.; Jaskari, M.; Kuběna, I.; Fintová, S.; Chlupová, A.; Karjalainen, L.P.; Polák, J. Cyclic deformation behaviour and stability of grain-refined 301LN austenitic stainless structure. In *MATEC Web of Conferences*; EDP Sciences: Les Ulis, France, 2018; Volume 165, p. 06005.

42. Järvenpää, A.; Jaskari, M.; Man, J.; Karjalainen, L.P. Austenite stability in reversion-treated structures of a 301LN steel under tensile loading. *Mater. Charact.* **2017**, *127*, 12–26. [CrossRef]
43. Järvenpää, A.; Jaskari, M.; Man, J.; Karjalainen, L.P. Stability of grain-refined reversed structures in a 301LN austenitic stainless steel under cyclic loading. *Mater. Sci. Eng. A* **2017**, *703*, 280–292. [CrossRef]
44. FEI Company. *MagellanTM XHR SEM User Manual*; FEI Company: Hillsboro, OR, USA, 2001.
45. Šakić, A.; Nanver, L.K.; van Veen, G.; Kooijman, K.; Vogelsamg, P.; Scholtes, T.L.M.; de Boer, W.; Wien, W.H.A.; Milosavljevic, S.; Heerkens, C.T.H.; et al. Versatile silicon photodiode detector technology for scanning electron microscopy with high-efficiency sub-5keV electron detection. In Proceedings of the 2010 International Electron Devices Meeting, San Francisco, CA, USA, 6–8 December 2010; pp. 31.4.1–31.4.4. [CrossRef]
46. FEI Company. *FEI Maps 2.5 SW Application User Guide*; FEI Company: Hillsboro, OR, USA, 2016.
47. Mikmeková, Š.; Yamada, K.; Noro, H. Dual-phase steel structure visualized by extremely slow electrons. *Microscopy* **2015**, *64*, 437–443. [CrossRef]
48. Sato, K.; Sueyoshi, H.; Yamada, K. Characterization of complex phase steel using backscattered electron images with controlled collection angles. *Microscopy* **2015**, *64*, 297–304. [CrossRef]
49. Marshall, P. *Austenitic Stainless Steels: Microstructure and Mechanical Properties*; Elsevier Applied Science Publishers: London, UK; New York, NY, USA, 1984; p. 29.
50. Ronneberger, O.; Fischer, P.; Brox, T. U-Net: Convolutional networks for biomedical image segmentation. In Proceedings of the 18th International Conference on Medical Image Computing and Computer-Assisted Intervention (MICCAI 2015), Munich, Germany, 5–9 October 2015; Part III 18. Springer International Publishing: Cham, Switzerland, 2015; pp. 234–241.
51. Gu, J.; Wang, Z.; Kuen, J.; Ma, L.; Shahroudy, A.; Shuai, B.; Liu, T.; Wang, X.; Wang, L.; Wang, G.; et al. Recent advances in convolutional neural networks. *Pattern Recognit.* **2018**, *77*, 354–377. [CrossRef]
52. Li, Z.; Liu, F.; Yang, W.; Peng, S.; Zhou, J. A survey of convolutional neural networks: Analysis, applications, and prospects. *IEEE Trans. Neural Netw. Learn. Syst.* **2022**, *33*, 6999–7019. [CrossRef]
53. Long, J.; Shelhamer, E.; Darrell, T. Fully convolutional networks for semantic segmentation. In Proceedings of the IEEE Conference on Computer Vision and Pattern Recognition (CVRP 2015), Boston, MA, USA, 7–12 June 2015; pp. 3431–3440.
54. He, K.; Zhang, X.; Ren, S.; Sun, J. Deep residual learning for image recognition. In Proceedings of the 2016 IEEE Conference on Computer Vision and Pattern Recognition (CVPR), Las Vegas, NV, USA, 27–30 June 2016; pp. 770–778.
55. Lin, T.-Y.; Dollár, P.; Girshick, R.; He, K.; Hariharan, B.; Belongie, S. Feature pyramid networks for object detection. In Proceedings of the IEEE Conference on Computer Vision and Pattern Recognition (CVPR), Honolulu, HI, USA, 21–26 July 2017; pp. 936–944.
56. Chaurasia, A.; Culurciello, E. LinkNet: Exploiting encoder representations for efficient semantic segmentation. In Proceedings of the 2017 IEEE Visual Communications and Image Processing (VCIP), St. Petersburg, FL, USA, 10–13 December 2017; pp. 1–4. [CrossRef]
57. Zhao, H.; Shi, J.; Qi, X.; Wang, X.; Jia, J. Pyramid scene parsing network. In Proceedings of the 2017 IEEE Conference on Computer Vision and Pattern Recognition (CVPR), Honolulu, HI, USA, 26 July 2017; pp. 6230–6239. [CrossRef]
58. Russakovsky, O.; Deng, J.; Su, H.; Krause, J.; Satheesh, S.; Ma, S.; Huang, Z.; Karpathy, A.; Khosla, A.; Bernstain, M.; et al. ImageNet large scale visual recognition challenge. *Int. J. Comput. Vis.* **2015**, *115*, 211–252. [CrossRef]
59. Paszke, A.; Gross, S.; Massa, F.; Lerer, A.; Bradbury, J.; Chanan, G.; Kileen, T.; Lin, Z.; Gimelshein, N.; Antiga, L.; et al. PyTorch: An imperative style, high-performance deep learning library. In *Advances in Neural Information Processing Systems 32, Proceedings of the Annual Conference on Neural Information Processing Systems 2019, Vancouver, BC, Canada, 8–14 December 2019*; NeurIPS 2019; Wallach, H.M., Larochelle, H., Beygelzimer, A., d'Alché-Buc, F., Fox, E.A., Garnett, R., Eds.; Neural Information Processing Systems Foundation, Inc.: La Jolla, CA, USA, 2019; pp. 8024–8035.
60. Li, X.; Sun, X.; Meng, Y.; Liang, J.; Wu, F.; Li, J. Dice loss for data-imbalanced NLP tasks. In Proceedings of the 58th Annual Meeting of the Association for Computational Linguistics, Online, 5–10 July 2020; Jurafsky, D., Chai, J., Schluter, N., Tetreault, J., Eds.; The Association for Computational Linguistics: Stroudsburg, PA, USA, 2020; pp. 465–476.
61. Wu, S.; Li, X.; Wang, X. IoU-aware single-stage object detector for accurate localization. *Image Vis. Comput.* **2020**, *97*, 103911. [CrossRef]

Disclaimer/Publisher's Note: The statements, opinions and data contained in all publications are solely those of the individual author(s) and contributor(s) and not of MDPI and/or the editor(s). MDPI and/or the editor(s) disclaim responsibility for any injury to people or property resulting from any ideas, methods, instructions or products referred to in the content.